ISSN 1330-3651 (Print), ISSN 1848-6339 (Online) https://doi.org/10.17559/TV-20250120002282
Original scientific paper

Employing the Improved PSO for the Multi-Objective Optimization of Sinusoidal Pole Wide Modulation PM Motors

Xiaoqing LIU*, Mingxia WANG, Liumin LUO, Xiyuan YUE

Abstract: To address the issues of high levels of back electromotive force harmonics and significant torque ripple in conventional surface-mounted permanent magnet motors, which are caused by the non-sinusoidal pole-air-gap magnetic density waveform, a sine-modulated pole PM motor has been designed. To achieve both high average torque and low torque ripple simultaneously, a multi-objective optimization approach that integrates the response surface method with an improved pso (particle swarm optimization) algorithm is employed. After presenting the magnetic modulation principle of the motor, finite element simulations and central composite experiments are conducted to obtain response values and establish a quadratic response surface regression model. Subsequently, employing this model, with torque ripple and average torque as optimization objectives, the enhanced multi-objective pso algorithm is applied to optimize the main structural parameters. The experimental findings compellingly illustrate that in the optimized sinusoidal extremely wide modulation PM motor, the torque ripple and cogging torque undergo remarkable reductions of 67.06% and 63.61% respectively. Concurrently, the utilization rate of the permanent magnet experiences a notable uptick of 6.11%. These outcomes serve as robust validation for the effectiveness and economic viability of the proposed methodology.

Keywords: finite element analysis; PM motor; PSO; torque ripple

1 INTRODUCTION

Surface-mount permanent magnet synchronous motors provide the advantages of high efficiency and reliability, and have become increasingly prevalent in the oil extraction sector in recent years [1-3]. With their application domain expanding rapidly, there is an increasing demand for the quality and performance of these motors. Traditional tile-shaped tablet stickers, featuring a rectangular magnetic momentum and a uniform air gap magnetic pole structure, produce a sinusoidal waveform of the no-load air gap magnetic flux density. This, in turn, affects the motor's stability. Consequently, increasing the density of the air gap magnetic flux and reducing torque pulsations are of significant importance [4, 5].

To reduce the torque of the permanent magnet synchronous motor, one can initiate improvements through the design and control strategy of the motor body. Optimizing the motor's structure by altering the shape of the permanent magnet is one effective method [6, 7]. The principle involves modifying the traditional magnetic pole by changing the shape of the permanent magnet and adjusting its thickness in the magnetic direction, thereby generating a magnetic field with a sine-like distribution in the air gap. Reference [8] introduces a novel eccentric magnetic pole structure to refine the air-gap magnetic flux density waveform. In Reference [9], an analytical model of the permanent magnet motor with non-uniform pole domain thickness was developed, deriving analytical expressions for the air gap magnetic flux density and cogging torque. These findings indicate that the non-uniform air gap structure created by altering the shape of the permanent magnet can effectively suppress magnetic dense harmonics in the motor and enhance the air gap's magnetic flux waveform.

The Pulse Width Modulation (PWM) waveform, also known as ultra-wide modulation technology, is utilized in motor drive control for shaping the magnetic fields of permanent magnets. Reference [10] applies polar width modulation segmentation technology to the table sticker motor, determining the structure and location of the permanent magnets across the entire rotor surface through theoretical calculations. The resulting air gap magnetic field waveform is more sinusoidal, effectively suppressing harmonic content within the air gap magnetic field.

In Reference [11], the ultra-wide modulated block technique was applied to the design of built-in permanent magnet synchronous motors. Reference [12] designed a permanent magnet synchronous motor with block magnetic poles and other wide-polar sine-stringed configurations, studying its inhibitory effect on air gap magnetic harmonics and cogging torque. The aforementioned studies divided the permanent magnets to achieve ultra-wide modulation, but did not further explore the use of pole cutting technology in conjunction with pole-wide modulation technology. Building upon this, this article investigates the effects of pole width adjustment technology on average torque and the suppression of torque pulse when the magnetic pole is cut.

Over the past few years, both domestic and international scholars have proposed various motor optimization design methods, including the Taguchi method, response surface method, genetic algorithm, and particle swarm optimization algorithm. However, these optimization objectives are often relatively simple, and the sole application of any one of the above methods has its limitations. Reference [13] optimized an axial magnetic flux permanent magnet motor, selecting a series of motor structural parameters based on experience and applying the Taguchi method and response surface method for optimization. However, this method exhibited poor multi-parameter cross-solving and optimization capabilities. Reference [14] used the hybrid particle swarm optimization algorithm to optimize the design of a low-speed and high-torque permanent magnet motor, achieving results that closely matched the design goals, though the global optimization ability was inadequate. Reference [15] employed the response surface method and particle swarm optimization algorithm to optimize the geometric parameters and oblique polar distribution of a permanent magnet driver with the goal of reducing cogging torque, but the optimization goal was singular. Reference [16] adopted orthogonal-particle swarm multi-objective optimization methods to ensure torque density and reduce torque pulse in optimizing the design of a permanent magnet bidding motor, yet the process was cumbersome and the efficiency low.

The unique rotor structure of the sine-string-wide-module motor proposed in this article necessitates consideration of many structural parameters during the optimization analysis process. The cross-impact of each parameter on the optimization goal increases the difficulty of motor optimization design, which is a complex nonlinear problem involving multiple optimization objectives. Traditional motor optimization design methods either have a single optimization goal, poor global optimization ability, or a complex process and low efficiency. Therefore, this paper takes average torque and torque ripple as the optimization objectives, combining the response surface method with the improved multi-objective particle swarm optimization algorithm (MOPSO) with an improved inertia weight. The advantages of different optimization methods are fully utilized, and the optimal structural size parameters of the proposed motor are ultimately determined. The design scheme before and after optimization is compared and analyzed to verify the feasibility and effectiveness of the proposed multi-objective optimization method.

2 MOTOR STRUCTURE AND WORKING PRINCIPLE

2.1 The Basic Structure of a Sinusoidal Extremely Wide Modulated Permanent Magnet Motor

This article examines an 18 slot, 20 pole SPMSM as an example. The SPMSM is utilized in the oil field of a deep well. It descends to a depth of 2000 meters underground through the sleeve. The harsh, high-temperature, and high-pressure environment of deep wells, along with the restrictions on the size of the pumping wellhead and casing, necessitate a motor stator with a small outer diameter, overall slimness, and a large length-to-diameter ratio. To ease fabrication and installation, the motor is segmented into shorter sections that can be connected, as depicted in Fig. 1.

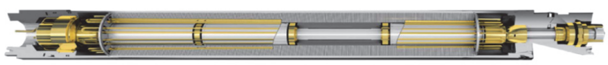

Figure 1 Schematic diagram of SPMSM

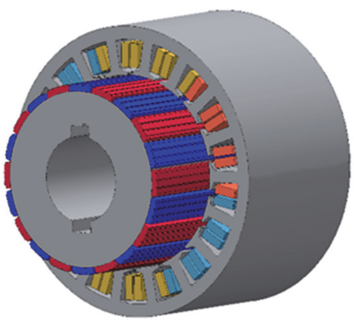

Figure 2 Structure of sinusoidal extremely wide modulated permanent magnet motor

The stator windings of a single-stage motor are connected in series, and its power is determined by the aggregate power of each motor. Based on the design theory and technical requirements of the motor, in conjunction with its unique structure and operational environment, the SPMSM discussed in this paper has an axial length of 4500 mm, comprised of nine 500 mm unit motors linked together. Tab. 1 presents the basic parameters of the motor, and the structure of the sinusoidal extremely wide modulated permanent magnet motor is illustrated in Fig. 2.

Table 1 Prototype parameters

Motor parameters	Value
rated power / kW	15
Rated voltage /V	380
Rated speed / (r.min−1)	400
Number of phases of the motor	3
Number of pole pairs	10
Slot	18
Inner diameter of the stator / mm	68
Outer diameter of the stator / mm	102.3
Rotor outer diameter / mm	62
Axial length / mm	4500
Insulation rating	H
Magnet material	N38UH

2.2 The Working Principle of Sinusoidal Extremely Wide Modulated Permanent Magnet Motor

Sinusoidal Pulse Width Modulation (SPWM) is a control method that adjusts the output voltage to approximate a sine wave by varying the pulse width of the PWM. During modulation, the intersection points of the sinusoidal modulation wave and the carrier triangle wave dictate the inverter's switching mode, resulting in a pulse sequence of equal amplitude and width. This sequence's fundamental wave aligns with the primary components of the sinusoidal modulated wave.

The sinusoidal width modulation structure can be viewed as a symmetrical array of magnetic teeth on the surface of the rotor magnetic poles, ensuring that the tooth width, tooth height, and the spacing between the magnetic teeth in the array adhere to the modulation relationship of SPWM technology. As depicted in Fig. 3, the height of the magnetic tooth is denoted by A, and the thickness of the magnetic base is represented by l_b.

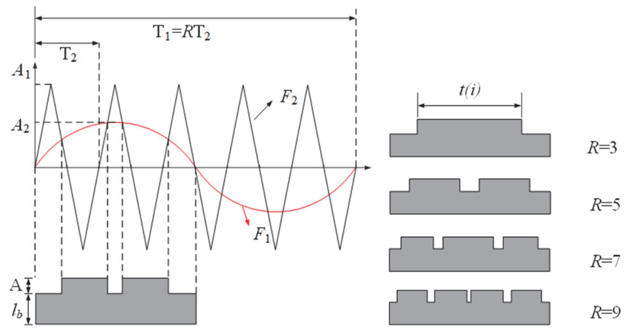

Figure 3 Magnetic pole parameters of sinusoidal pole width modulation structure

The tooth width is correlated with the sinusoidal function F_1 with a spatial period of T_1 and the trigonometric carrier function F_2 with a spatial period of T_2. The formula for the width of the ith tooth is presented in Eq. (1).

$$t(i) = \frac{1 + M\sin(a(i))}{2} T_2$$
$$a(i) = \frac{2\pi(i - 0.25)}{R}, i = 1, 2, \ldots, (R-1)/2 \tag{1}$$

in Eq. (1): R is the cycle ratio, $R = T_1/T_2$; M is the modulation ratio, $M = A_1/A_2$, where the amplitude of A_1 and A_2 is the amplitude of F_1 and F_2, respectively.

From Eq. (1), the intersection of the sine function F_1 and the triangular wave function F_2 is:

$$p(n)=\begin{cases}0, & n=0\\ (n-\frac{1}{4})T_2-\frac{1}{2}t(\frac{n+1}{2}), & n=1,3,5,...,R-2\\ (n-\frac{5}{4})T_2-\frac{1}{2}t(\frac{n}{2}), & n=2,4,6,...,R-1\\ \frac{T_1}{2}, & n=R\end{cases} \tag{2}$$

Depending on the intersection position, the distribution function of the magnetic tooth array is shown in Eq. (3):

$$p_s(n)=\begin{cases}0, & n=0\\ \omega_o+\omega_m\dfrac{p\left(n+\frac{R-1}{2}\right)}{p(R)}-\dfrac{\pi}{2N_p}, & 1\le n\le\frac{R+1}{2}\\ \omega_o+\omega_m\dfrac{p\left(n-\frac{R+3}{2}\right)}{p(R)}+\dfrac{\pi}{2N_p}, & \frac{R+3}{2}\le n\le R+1\\ \dfrac{\pi}{N_p}, & n=R+2\end{cases} \tag{3}$$

In Eq. (3): ω_0 is the gap length of adjacent magnetic poles, ω_m is the pole width, N_p represents the number of pole pairs.

Fig. 4 depicts a schematic diagram of the ideal structure beneath a magnetic pole. The shape of the magnetic pole is determined according to $p_s(n)$ and the height of the magnetic tooth A. The yellow arrows in Fig. 4 indicate the direction of parallel magnetization, β_q, the offset angle of the magnetic tooth in relation to the magnetic pole's center line, and l_g is the minimum radial air gap length.

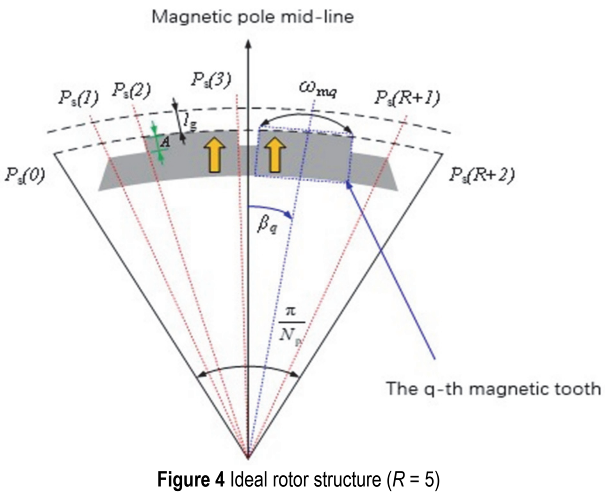

Figure 4 Ideal rotor structure (R = 5)

Grounded in the principles of air-gap magnetic field modulation [17, 18], when the magnetic teeth on the surface of the magnet are periodically distributed, the expression of the radial air-gap magnetic flux density $B_{pm}(r, \theta)$ on the SPWM-shaped pole with q blocks at each pole is shown in Eq. (4):

$$\begin{aligned}B_{pm}(r,\theta)=&\sum_{q=1}^{R}\sum_{n=1,3,5}^{\infty}\left\{\left[\frac{nN_pB_rM_{pwm,nq}}{\mu_R\left((nN_p)^2-1\right)}\right]\times\right.\\ &\times\left[\frac{\left(nN_p-1\right)+2\left(\frac{R_{si}}{R_{mq}}\right)^{nN_p+1}+\left(nN_p+1\right)\left(\frac{R_{si}}{R_{mq}}\right)^{2nN_p}}{\frac{\mu_r+1}{\mu_r}\left[1-\left(\frac{R_{si}}{R_{pi}}\right)^{2nN_p}\right]-\frac{\mu_R-1}{\mu_R}\left[\left(\frac{R_{mq}}{R_{pi}}\right)^{2nN_p}-\left(\frac{R_{si}}{R_{mq}}\right)^{2nN_p}\right]}\right]\times\\ &\left.\times\left[\left(\frac{r}{R_{pi}}\right)^{nN_p-1}\left(\frac{R_{mq}}{R_{pi}}\right)^{nN_p+1}+\left(\frac{R_{mq}}{R_{si}}\right)^{nN_p+1}\right]\cos\left(nN_p\theta\right)\right\}\end{aligned} \tag{4}$$

in Eq.(4): B_r is the remanence density of the permanent magnet; μ_r is the relative permeability of the permanent magnet; R_{si} is the outer radius of the rotor; R_{mq} is the radius of the magnet; R_{pi} is the inner radius of the stator; q and n denote the modulation coefficients of harmonics.

Considering the offset angle β_q of the magnet, the Fourier coefficient $M_{pwm,nq}$ is:

$$M_{pwm,nq}=\frac{4}{n\pi}\sin\left(\frac{nN_pw_{mq}}{2}\right)\cos\left(nN_p\beta_q\right) \tag{5}$$

After considering the effects of flux leakage and cogging, the expression of the magnetic flux density of the air gap is:

$$\begin{aligned}B_g(r,\theta)=\sigma_0\tilde{\lambda}(\theta)B_{pm}(r,\theta)=\\ =\sigma_0\frac{l_g+\frac{l_b+A}{\mu_r}}{l_g+g(\theta)+\frac{l_b+A}{\mu_r}}B_{pm}(r,\theta)\end{aligned} \tag{6}$$

In Eq. (6), σ_0 is the magnetic leakage coefficient in the magnetic circuit model.

Considering the stator slot, the equivalent air gap length $g(\theta)$ is shown in Eq. (7):

$$g(\theta)=\begin{cases}\frac{\pi}{2}R_{pi}\left(\frac{\alpha_0}{2}-\left|\theta-n\alpha_t\right|\right), & -\frac{b_0}{2}+n\alpha_t<\theta<\frac{b_0}{2}+n\alpha_t\\ 0, & \text{elsewhere}\end{cases} \tag{7}$$

In Eq. (7), α_0 is the groove width; α_t is the tooth width; n = 0, 1, 2, …, N_s−1; N_s is the slot number.

3 MULTI-OBJECTIVE OPTIMIZATION DESIGN OF ELECTRIC MOTORS

The multi-objective optimization method for the sinusoidal extremely wide modulated permanent magnet motor, as proposed in this paper, is founded on the response surface method and the MOPSO algorithm. Consequently, a brief description of both the response surface method and the MOPSO algorithm is provided initially.

3.1 Response Surface Method

The fundamental concept of the response surface method is to ascertain the intricate implicit functional relationship between the response and the variables by regressing and fitting a series of sample points based on the system's responses at various sampling points. Since the response value of the experiment cannot be obtained during the design stage, the finite element simulation results are used as the system's response. The second-order response surface model is expressed as shown in Eq. (8).

$$y=\beta_0+\sum_{j=1}^{n}\beta_j x_j+\sum_{j=1}^{n}\beta_{jj}x_j^2+\sum_{i=1}^{n}\sum_{j=i+1}^{n}\beta_{ij}x_i x_j+\varepsilon \tag{8}$$

In Eq. (8): y is the objective function; β is the regression coefficient, which is also the value to be evaluated in the response surface model; x_j is an experimental variable; n is the number of experimental variables; ε is the error.

The allocation of sample points throughout the design space plays a crucial role in determining the precision of the response surface model's fit. Optimal selection of these points can lead to increased fitting precision and heightened optimization efficiency. This paper adopts the central composite design (CCD) method for point selection, facilitating a thorough analysis and study with a reduced number of experiments, thus enhancing efficiency over traditional full factor design approaches.

3.2 Improvement of the MOPSO Algorithm

Once the optimization objective function has been clearly defined through the application of the response surface method, Multi-objective Particle Swarm Optimization (MOPSO) is utilized to avoid design objective conflicts and to perform optimization. Like the traditional single-objective PSO algorithm, MOPSO employs a swarm of particles to explore the multi-dimensional search space in order to identify the optimal solution for the problem at hand. The velocity and position of the particles are iterated to move the global particle swarm towards the optimal position of the objective function [19]. The updated formula for velocity and position is shown in Eq. (9):

$$v_{ij}^{k+1}=\omega v_{ij}^{k}+c_1 r_1\left(P_{ij}^{k}-x_{ij}^{k}\right)+c_2 r_2\left(G_{ij}^{k}-x_{ij}^{k}\right)$$
$$x_{ij}^{k+1}=x_{ij}^{k}+v_{ij}^{k+1} \tag{9}$$

In Eq. (9): i is the particle label; j is the spatial dimension of the particle; k is the current number of iterations; v_{ij}^{k+1} is the j-dimensional velocity component of particle i when iteration k + 1 times; x_{ij}^{k+1} is the j dimensional position component of particle i when iterative k + 1 times; P_{ij}^{k} is the best position of particle i in the j-dimensional space when it is iterated k times; G_{ij}^{k} is the global optimal position of particle i in the j dimensional space when it is iterated k times; c_1, c_2 are the Group learning factor, and c_1 > 0, c_2 > 0; r_1 and r_2 are uniformly distributed random numbers within [0,1]. ω is the inertia weight coefficient, and $\omega \geq 0$.

Considering the issue that the traditional MOPSO algorithm tends to converge prematurely to local optima, resulting in low accuracy of results, combined with the existing optimization algorithms, this paper proposes a nonlinear decreasing weight strategy, which can effectively balance the local search and global search capabilities, as shown in Eq. (10). The inertia weight as a function of the number of iterations is shown in Fig. 5.

$$\omega(k)=\omega_{\text{start}}-\left(\omega_{\text{start}}-\omega_{\text{end}}\right)\cdot\left(e-e^{-45\left(k/G_{\max}\right)^3}\right) \tag{10}$$

In Eq. (10): ω_{start} and ω_{end} represent the values of the initial and final inertia weights, respectively; $G_{\max}$ is the maximum number of iterations.

As illustrated in Fig. 5, the improved method demonstrates superiority over the linear decreasing strategy of inertia weight. In the initial stages of the search, the inertia weight is maintained at a high value for a period, which favors global search. Subsequently, the inertia weight decreases rapidly, allowing it to be maintained at a low value for a period in the later stages of the search, which enhances local refinement search. This approach increases the likelihood of locking onto the optimal solution and effectively balances the global and local search capabilities of MOPSO.

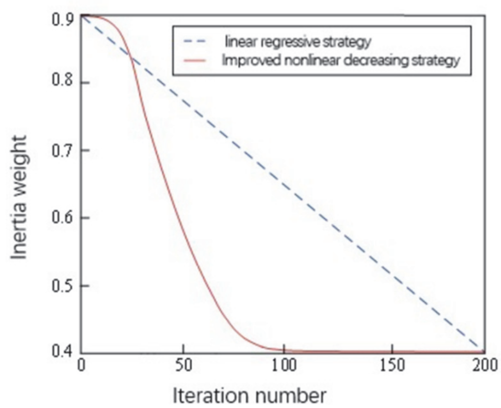

Figure 5 Comparison of inertia weight curves

To verify the superiority of the proposed optimization method, the MOPSO algorithm with fixed weights and linearly decreasing weights is compared with the improved MOPSO algorithm presented in this paper. The standard test function ZDT1 was selected, the number of particle swarm populations was 40, and the number of iterations was 200. The optimization algorithms with three different weight update methods were repeatedly run 50 times, and the mean and variance of the generational distance (GD), spatial index (SP) and runtime of the three algorithms were obtained to measure the convergence, diversity and operation efficiency of the optimization algorithms, as shown in Tab. 2.

Table 2 Comparison results of optimization algorithms

index	Fixed weights	Weight Linear Decrease	Improved weighting Update method
GD mean	9.03 × 10^{-4}	6.81 × 10^{-4}	4.18 × 10^{-4}
GD variance	1.58 × 10^{-4}	1.97 × 10^{-4}	1.13 × 10^{-4}
SP mean	9.21 × 10^{-3}	7.26 × 10^{-3}	4.83 × 10^{-3}
SP variance	1.46 × 10^{-3}	8.22 × 10^{-4}	1.13 × 10^{-3}
Runtime mean	4.61 × 10^{-1}	4.47 × 10^{-1}	4.06 × 10^{-1}
Runtime variance	5.12 × 10^{-3}	3.59 ×10^{-3}	2.62 ×10^{-3}

As indicated by Tab. 2, apart from the SP variance index, the proposed improved MOPSO algorithm outperforms both the MOPSO algorithm with fixed weights and the one with linearly decreasing weights. This confirms that the improved MOPSO algorithm exhibits superior convergence, diversity, and operational efficiency.

3.3 Multi-Objective Optimization Process

The flow of the proposed optimal design method for sinusoidal, extremely wideband modulated motors is illustrated in Fig. 6.

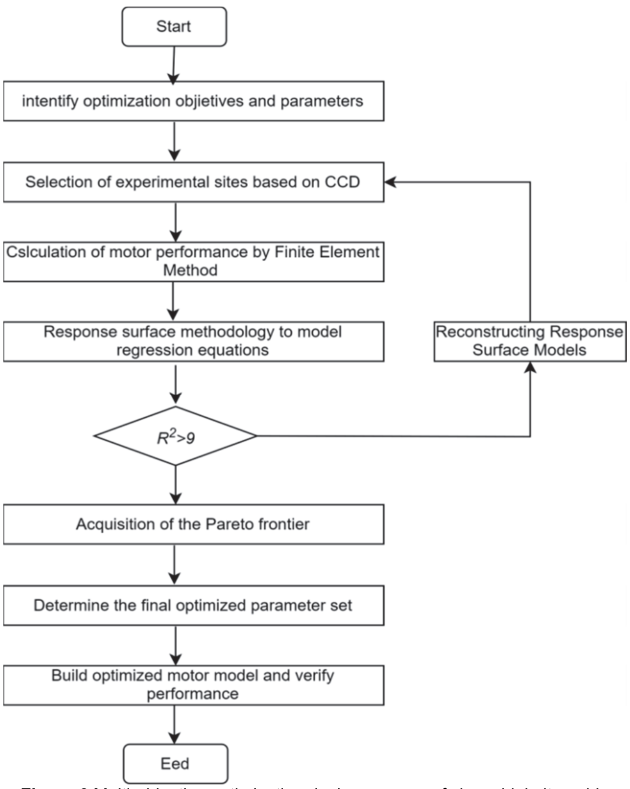

Figure 6 Multi-objective optimization design process of sinusoidal ultra-wide modulated motor

3.3.1 Determine the Optimization Objectives and Optimization Parameters

To compare the performance of the motor before and after pole cutting using sinusoidal pole width modulation technology, all the original size of the motor is retained. This paper selects the magnetic pole shape parameters like the period ratio R, the modulation ratio M, the magnetic tooth height A, and the magnetic pole width ω_m as the optimization parameters, and the average torque and torque ripple are taken as the objective functions of the motor optimization, and the optimization problem can be expressed as:

$$\min \begin{cases} f_1(x) = -T_a \\ f_2(x) = -T_r \end{cases} \tag{11}$$

$$\text{s.t} \begin{cases} 0.3 \le A \le 0.5 \\ 5 \le R \le 9 \\ 0.7 \le M \le 0.9 \\ 16.665 \le \omega_m \le 17.665 \end{cases} \tag{12}$$

In Eq. (11): Ta is the average torque; T_r is torque ripple.

3.3.2 Response Surface Method Modeling

In this paper, CCD method was used. The center composite Design was carried out by Design-Expert. and a total of 30 groups of tests were carried out. Test No. 25 - 30 was repeated test at the center point, aiming to provide better prediction ability near the center point.

This paper utilizes ANSYS finite element analysis software to conduct experiments and establishes a second-order regression model based on the simulation outcomes. The levels of the design variable factors are presented in Tab. 3, while the test arrangement and simulation results are depicted in Tab. 4.

Table 3 Level of the design variable factor

Factor	Level		
	−1	0	1
A	0.3	0.4	0.5
R	5	7	9
M	0.7	0.8	0.9
ω_m / deg	16.665	17.165	17.665

Table 4 Test arrangement and simulation results

Group number	Factor				T_a / N.m	T_r / %
	$X1(A)$	$X2(R)$	$X3(M)$	$X4(\omega_m)$		
1	−1	−1	−1	−1	458.92	2.11
2	1	−1	−1	−1	478.23	3.33
3	−1	1	−1	−1	458.38	3.14
4	1	1	−1	−1	479.73	3.84
5	−1	−1	1	−1	463.02	2.11
6	1	−1	1	−1	487.91	3.38
7	−1	1	1	−1	463.19	3.04
8	1	1	1	−1	484.97	2.92
9	−1	−1	-1	1	459.50	3.09
10	1	−1	-1	1	477.91	2.63
11	−1	1	-1	1	462.75	4.54
12	1	1	-1	1	486.06	4.36
13	−1	−1	1	1	466.44	3.45
14	1	−1	1	1	487.37	3.21
15	−1	1	1	1	466.92	4.50
16	1	1	1	1	492.39	4.84
17	−1	0	0	0	463.49	3.92
18	1	0	0	0	485.16	4.19
19	0	−1	0	0	472.81	2.69
20	0	1	0	0	472.75	4.34
21	0	0	−1	0	470.94	4.43
22	0	0	1	0	478.30	3.85
23	0	0	0	−1	470.33	2.95
24	0	0	0	1	476.72	4.61
25	0	0	0	0	474.66	4.11
26	0	0	0	0	475.13	4.09
27	0	0	0	0	473.72	4.24
28	0	0	0	0	475.64	4.06
29	0	0	0	0	472.99	4.01
30	0	0	0	0	473.74	4.16

In the CCD method, each factor is categorized into three levels: −1, 0, and 1. The value 0 signifies the midpoint, whereas 1 and −1 denote the highest and lowest values, respectively.

Based on the outcomes of the finite element simulation calculations, the model has been fitted, and the final regression equations are presented in Eq. (13) and Eq. (14). The motor performance and response surface model's approximation is denoted by the multiple correlation coefficient, R^2. When R^2 approaches 1, it signifies that the model's accuracy is higher. The analysis found that the R^2 of the two models was 0.9943 and 0.9764, respectively, which were higher than 0.9. The outcomes demonstrate that the linear correlation between the response value and the independent variables is statistically significant, and it exhibits favorable applicability and a robust correlation.

$$\begin{aligned} T_a = & -74 - 65A - 9.56R - 182M + 69.7\omega_m + \\ & +21.5A^2 - 0.333R^2 + 51M^2 - 2.35\omega_m{}^2 + \\ & +1.72AR + 84.8AM + 4.58A\omega_m - \\ & -3.91RM + 0.99R\omega_m + 7.42M\omega_m \end{aligned} \tag{13}$$

$$\begin{aligned} T_r = & -0.32 + 0.96A - 0.0232R - 0.476M + 0.377\omega_m - \\ & -0.004A^2 - 0.001361R^2 + 0.083M^2 - 0.0112\omega_m{}^2 - \\ & -0.00133AR - 0.0401AM - 0.0526A\omega_m - \\ & -0.00301RM + 0.002974R\omega_m + 0.0219M\omega_m \end{aligned} \tag{14}$$

The response surface of the optimization target in relation to the optimization parameters is depicted in Fig. 7 and Fig. 8. Fig. 7 illustrates that as the value of A increases, the average torque and torque ripple gradually rise. Regarding the parameter M, an increase in its value initially leads to a decrease in torque ripple, followed by an increase, while the average torque experiences a marginal rise. Observing Fig. 8, it becomes clear that as R grows, the average torque also ascends, yet the torque ripple follows a pattern of initial increase and subsequent decline. For the parameter ω_m, both the average torque and torque ripple increase as it increases. From the analysis presented, it becomes clear that the response surface model possesses extreme values and the optimization parameters define an optimal range. Nonetheless, the optimal value range for each response surface model is distinct. Consequently, to avert conflicts among design goals, the application of a multi-objective intelligent optimization algorithm is required to discover the Pareto optimal solution for the multi-objective optimization issue.

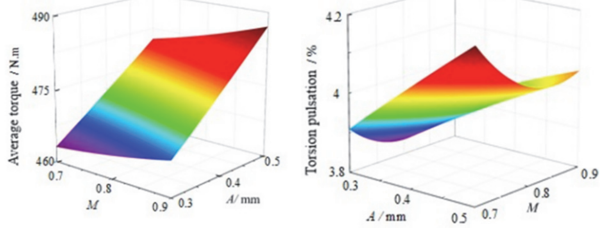

(1) The average torque response changes (2) Torque ripple response changes

Figure 7 The response of the optimization target under structural parameters A and M

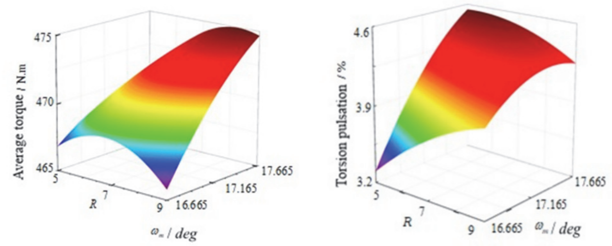

(1) The average torque response changes (2) Torque ripple response changes

Figure 8 The response of the optimization target under the structural parameters R and ω_m

3.3.3 Improved MOPSO Optimization

The enhanced MOPSO algorithm, as outlined in Section 2.2, is employed to refine the regression equation yielded by the response surface methodology. The optimization process was executed with remarkable speed. The outcomes of the global Pareto non-inferior solution distribution achieved through the enhanced pso algorithm are depicted in Fig. 9.

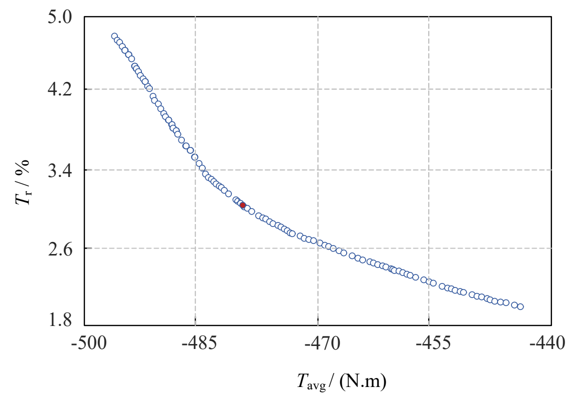

Figure 9 Pareto frontier diagram

In Fig. 9, each circle represents a non-inferior solution in the set of Pareto's optimal solutions, and the combination of all non-inferior solutions outlines the Pareto front. Considering the spatial distribution trend of the Pareto non-inferior solution set of the motor, the chosen optimal solution is denoted by a red dot in the diagram, as this position significantly diminishes the torque ripple while maintaining torque. Tab. 5 compares the results of the multi-objective optimization with the original design.

Table 5 Comparison of the multi-objective optimization results with the original design results

parameter	Initial value	Optimized value
A / mm	0.5	0.48
R	—	7
M	—	0.84
ω_m / deg	17.165	17.554

4 ANALYSIS OF OPTIMIZATION RESULTS

To ascertain the dependability and efficacy of the suggested optimization technique, this study develops a representation of the motor in its pre and post-optimization states within finite element analysis software, and conducts a comparative analysis of their electromagnetic properties.

The torque ripple is examined via an analytical method to yield:

$$T_{\mathrm{r}}=\frac{-\mu_{\mathrm{air}}}{l_{\mathrm{g}}}N_{\mathrm{p}}\,\mathrm{L}\,\pi\left(R_{\mathrm{si}}+l_{\mathrm{g}}\right)\cdot \cdot\sum_{\substack{h=6m\pm1\\ m=1,2,3,\cdots}}^{\infty}\left[hF_{sh}F_{rh}\sin\left((h\pm1)\omega_{\mathrm{e}}t\mp\gamma_{d}\right)\right] \tag{15}$$

In Eq. (15): μ_{air} is the permeability of air; L is the axial length of the motor; F_{sh} is the magnetic electromotive force coefficient of the h th stator; F_{rh} is the magnetic electromotive force coefficient of the h-th rotor; ω_{e} is the angular velocity; t is the time; γ_{d} is the current angle of the d axis; m is the number of phases of the motor.

From Eq. (15), it is evident that torque ripple is produced by the 6m ± 1 th harmonic, with the 5 th and 7 th harmonics exerting the most significant influence. Fig. 10 depicts the contrast in no-load airgap flux density before and after optimization. The outcomes of the Fourier analysis are presented in Fig. 11, indicating that the amplitudes of the 5 th and 7 th harmonics of the optimized no-load air gap magnetic flux density have been substantially diminished, which serves to effectively curb the harmonics of the air gap magnetic density.

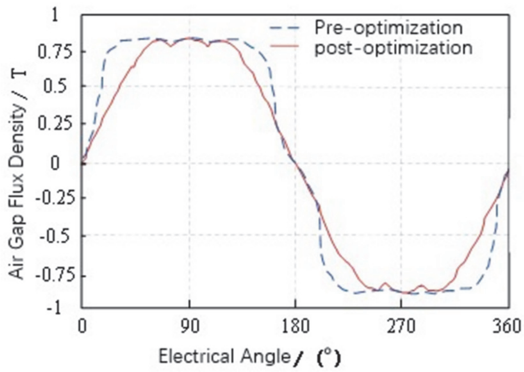

Figure 10 Comparison of waveforms of magnetic flux density in the no-load air gap

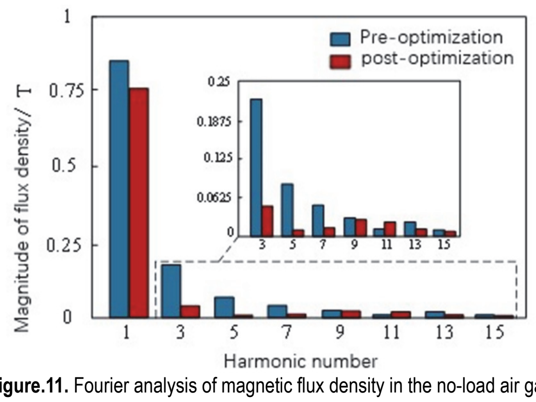

Figure.11. Fourier analysis of magnetic flux density in the no-load air gap

Fig. 12 depicts the alteration in the motor's cogging torque, which has diminished from 3.27 N·m to 1.19 N·m following optimization, marking a 63.61% reduction. To a certain extent, this diminishment in cogging torque can cause a reduction in the motor's torque ripple.

Referencing Fig. 13, the average torque before the optimization process was 493.74 N·m, and post-optimization, it has been reduced to 482.79 N·m, a decrease of 2.21%. The torque ripple of the motor before optimization was 8.44%, but after optimization, it has been cut down to 2.78%. It is apparent that the optimization has, without compromising the motor's average output torque, reduced the torque ripple by 67.06% compared to the motor's initial state. The simulation data supports the efficiency of the multi-objective optimization strategy.

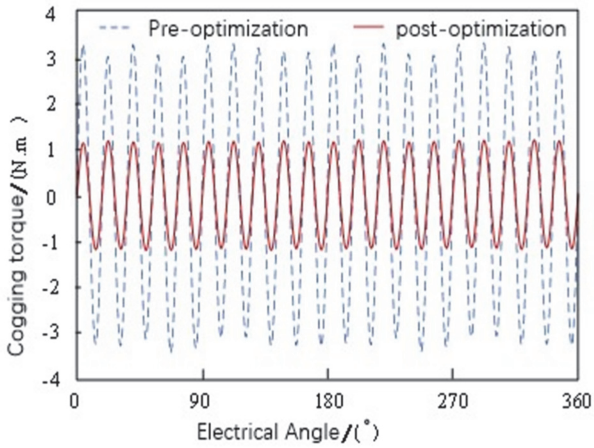

Figure 12 Comparison of cogging torque waveforms

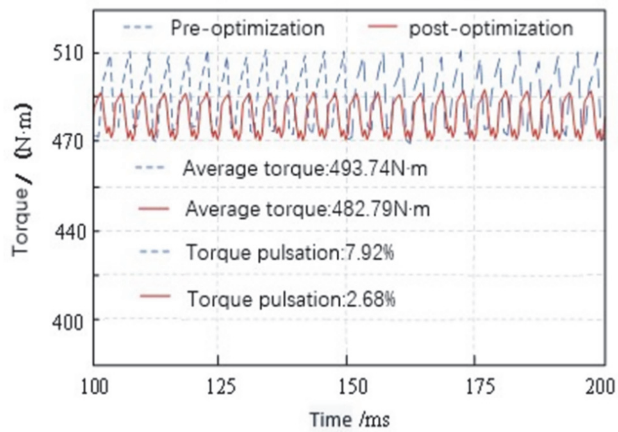

Figure 13 Comparison of torque waveforms before and after optimization

After calculation, it can be found that the amount of permanent magnet material used in the original motor is 100.64 cm^3, and the permanent magnet consumption material used in the optimized motor is 92.54 cm^3, which is reduced by 8.05%. The utilization rate of permanent magnet materials, which indicates how efficiently these materials are used, is directly linked to the motor's cost. The definition of its expression is:

$$\eta_{\mathrm{N}}=\frac{T_{\mathrm{a}}}{V_{\mathrm{N}}} \tag{16}$$

In Eq. (16): V_{N} is the amount of permanent magnet and η_{N} is the utilization rate of permanent magnet.

It is estimated that the permanent magnet usage efficiency of the motor has improved from 4.91 N·m/cm³ pre-optimization to 5.21 N·m/cm³ post-optimization, marking a 6.11% enhancement. Tab. 6 illustrates the performance metrics of the motor before and after the optimization process.

Table 6 Comparison of the performance of the motor before and after optimization

Performance metrics	Before optimization	After optimization	Changes before and after optimization
Average torque / N·m	493.74	482.79	10.95↓
Torque ripple / %	8.44	2.78	5.66 ↓
Cogging torque/ (N·m)	3.27	1.19	2.08 ↓
permanent magnet consumption material / cm^3	100.64	92.54	8.1 ↓
The utilization rateof permanent magnet / N·m/cm^3	4.91	5.21	0.3 ↑

5 EXPERIMENTAL ANALYSIS

To ascertain the viability of design optimization, it is necessary to conduct tests on the motor. Large oil motors are expensive and have extended production cycles. SPMSM is composed of 9 500 mm unit motors. In order to reduce economic costs and conduct technical verification, the author uses a 500 mm unit motor as a prototype to do a test. The test platform is illustrated in Fig. 14.

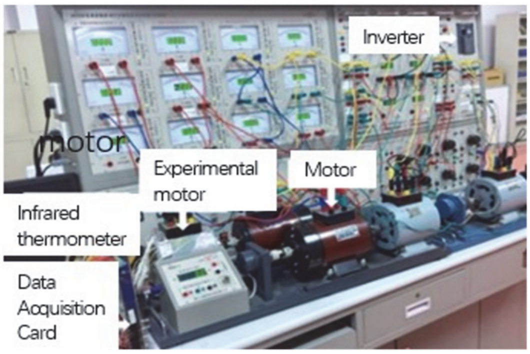

Figure 14 Test platform

The temperature of the control experimental platform was raised to the ambient temperature 100 °C by using a heat gun, and the prototype was tested. The comparison between the measured output torque results of the prototype and the simulation results is shown in Fig. 15. From the results, it can be seen that the average torque of the output is 54.16 N·m; The torque ripple is 3.01%, which is within a reasonable range of error from the optimization result.

To ensure the motor design's effectiveness and dependability, the temperature rise of the motor after stable operation was considered through the test, and the temperatures at the winding and rotor were measured by using a K-type thermocouple embedded in the end of the winding and an infrared thermometer, respectively, and the temperature rise test curve is shown in Fig. 16. It is evident that as the running time increases, the temperature of each motor component gradually stabilizes, with the maximum temperature reaching 157.63 °C, located in the winding section. and the maximum temperature of the rotor permanent magnet is 138.92 °C, which remains within the insulation specifications and the peak operating temperature of the permanent magnet, satisfying the requirements for the motor's enduring, secure, and stable performance.

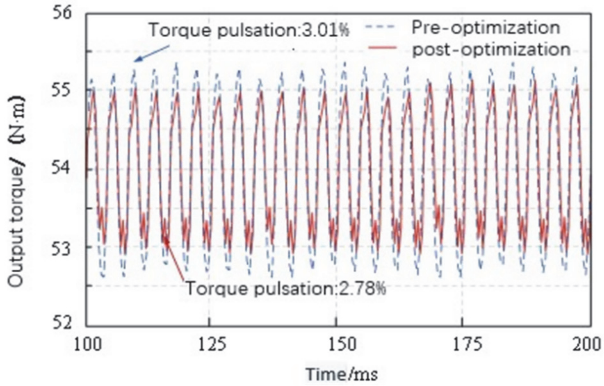

Figure 15 Torque comparison results

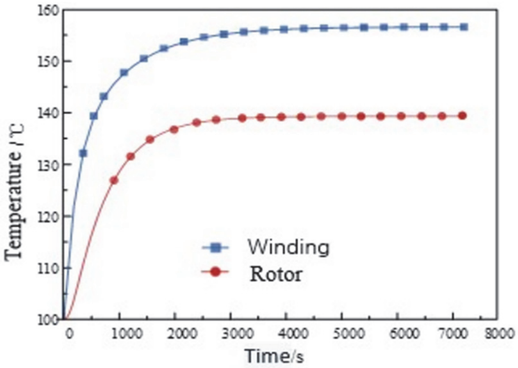

Figure 16 Temperature rise test results

6 CONCLUSION

To improve the performance of permanent magnet motors, a sinusoidal pole width modulated pole structure is suggested, and the pole surface distribution function is established. A multi-objective optimization design algorithm, which integrates the response surface method and an enhanced MOPSO algorithm, was utilized to refine the design. The motor's performance was assessed using finite element simulation both before and after optimization, and its efficacy was later confirmed through prototype testing. The following conclusions were then drawn:

(1) Compared to the conventional tile-shaped surface-mount permanent magnet motor, the sinusoidal ultra-wide modulated motor's average torque has decreased from 493.74 N·m to 482.79 N·m, a reduction of 2.21%. Furthermore, the torque ripple has diminished from 8.44% to 2.78%, a decrease of 67.06%. The cogging torque has also been reduced from 3.27 N·m to 1.19 N·m, a decrease of 63.61%. These enhancements effectively control torque ripple while maintaining the motor's average output torque.

(2) Compared to the initial motor design, the enhanced motor model exhibits a decrease in permanent magnet usage from 100.64 cm^3 to 92.54 cm^3, marking an 8.05% reduction. Furthermore, there's a 6.11% improvement in the efficiency of permanent magnet utilization, which contributes to a decrease in the motor's production expenses.

7 REFERENCES

[1] Zhao, S. H., Chen, J. H., & Zhang, C. (2022).Analytical Calculation of Magnetic Field of Permanent Magnet Synchronous Motor with Uneven Air Gap Structure.

Transactions of China Electrotechnology Society, 37(14), 3502-3513.

[2] Silvia, D., Michele, M., Fabio, D'A., Daniele, K., & Federico, S. (2024). Multiphysics Modeling and Simulation of Integrated Electric Propulsion System for Ship Dynamic Positioning. *IEEE Transactions on Industry Applications, 60*(3), 4958-4967. https://doi.org/10.1109/tia.2024.3355869

[3] Ding, Z., Wu, X. Z., Chen, C. T., & Yuan, X. B. (2023). Magnetic Field Analysis of Surface-Mounted Permanent Magnet Motors Based on an Improved Conformal Mapping Method. *IEEE Transactions on Industry Applications, 59*(2), 1689-1698. https://doi.org/10.1109/tia.2022.3228509

[4] Xia, W., Wang, K., & Zhang, J. Y. (2019). Torque Ripple Suppression of Permanent Magnet Synchronous Motor With Harmonic Shaped Rotors Based on Resonance Controllers. *Proceedings of the CSEE, 39*(18), 5499-5508+5598.

[5] Gao, M. Z., Yang, X. Y., & Jiang, S. Y. (2023). The Method for Reducing Cogging Torque by Suitable Selection of the Pole-arc Coefficient and Rotor Step Skewing in Five-phase Permanent Magnet Motor. *Proceedings of the CSEE, 43*(22), 8922-8935.

[6] Ji, J. P., Hua, Z. G., & Hu, X. L. (2014). Optimal design of branch topologies of passive power filter based on PSO. Power Electronics Technology. *Journal of Xi'an University of Technology, 30*(2), 231-237.

[7] Qi, X. D., Gao, F. Y., & Li, X. F. (2020). Optimized design of new eccentric poles for surface-mounted permanent magnet synchronous motors. *Journal of Electronic Measurement and Instrumentation, 34*(8), 93-100.

[8] Ni, Y. Y., Wang, L., & Wang, Q. J. (2020). Modeling and analysis of convex unequal-thickness pole permanent magnet motor. Modeling and Analysis of Permanent Magnet Machines with Salient Shape Unequal Thickness Magnets. *Transactionsof China Electrotechnology Society, 35*(11), 2406-2414.

[9] An, Y. J., Wen, H. L., & An, H. (2012). Magnetic Field Analysis and Experiment of Sinusoidal Magnetic PoleModulation Permanent Magnet Machine. *Transactionsof China Electrotechnology Society, 27*(11), 111-117. https://doi.org/10.19595/j.cnki.1000-6753.tces.2012.11.015

[10] Chaithongsuk, S., Nahid-Mobarakeh, B., Takorabet, N., Caron, J. P., & Meibody-Tabar, F. (2010). Optimal design of PM motors to achieve efficient flux weakening strategy in variable speed control applications. *The XIX International Conference on Electrical Machines.* ICEM, 1-6. https://doi.org/10.1109/icelmach.2010.5607858

[11] Zhu, Y. X., Zhang, G. F., & Qian, X. (2019). Optimum Design of Permanent Magnet Motor Based on Pole Equal Width and Thickness Modulation. *Micromotor, 52*(12), 34-38+48.

[12] Shangguan, X. F. & Wang, Y. C. (2017). Optimization of axial flux permanent magnet synchronous generator. *Electronic Measurement Technology, 40*(9), 45-52.

[13] Guo, X., Zhang, B. Y., & Feng, G. H. (2018). Multi-objective optimization of low speed high torque direct drive PMSM based on hybrid particle swarm optimization. *Journal of Mechanical & Electrical Engineering, 35*(11), 1214-1219.

[14] Shi, S. N. & Wang, D. Z. (2015). Magnet Skewing Optimization Method for Reducing Cogging Torque in Permanent Magnet Drive. *Transactions of China Electrotechnology Society, 30*(22), 27-32.

[15] Yang, Q. L., Guo, S. H., & Song, B. L. (2023). Multi-objective Orthogonal Particle Swarm Optimization of Permanent Magnet Vernier Motor. *Mechanical Science and Technology for Aerospace Engineering, 42*(12), 1996-2002.

[16] Cheng, M., Wen, H. H., & Hua, W. (2021). General Airgap Field Modulation Theory for Electrical Machines and Its Typical Applications. *Proceedings of the CSEE, 41*(24), 8261-8283.

[17] Zhu, Z. Q., Howe, D., Bolte, E., & Ackermann, B. (1993). Instantaneous magnetic field distribution in brushless permanent magnet DC motors. I. Open-circuit field. *IEEE Transactions on Magnetics, 29*(1), 124-135. https://doi.org/10.1109/20.195557

[18] Hao, Y. C., Zheng, J. H., & Liu, J. F. (2021). Multi-objective optimization of absorbing materials filled with graphene and magnetic particles based on MOPSO. *Journal of Xi'an University of Technology, 37*(4), 550-554.

[19] Cao, Z. Z., Zhang, Z., & Liu, J. L. (2020). Techniques of Torque Ripple Reduction for Outer-rotor Surface-mounted Permanent Magnet Synchronous Motor. *23rd International Conference on Electrical Machines and Systems (ICEMS)*, 494-497. https://doi.org/10.23919/icems50442.2020.9290813

Contact information:

Xiaoqing LIU
(Corresponding author)
School of Mechanical and Electrical Engineering,
Zhoukou Normal University,
Zhoukou 466000, China
E-mail: liuxiaoqing_zknu@163.com

Mingxia WANG
School of Mechanical and Electrical Engineering,
Zhoukou Normal University,
Zhoukou 466000, China
PLA Army Special Operations Academy Department of Mechanical and Electrical Engineering Guilin 541000, China

Liumin LUO
School of Mechanical and Electrical Engineering,
Zhoukou Normal University,
Zhoukou 466000, China

Xiyuan YUE
Xuchang Kaipu Testing Research Institute Co., LTD, Xuchang 461001, China